Title

Desalinating a real hyper-saline pre-treated produced water via direct-heat vacuum membrane distillation

Authors

Liu, Yiming
Wang, Jingbo
Jung, Bongyeon
et al.

Publication Date

2022-06-01

DOI

10.1016/j.watres.2022.118503

Desalinating a Real Hyper-Saline Produced Water via Direct-Heat Vacuum Membrane Distillation

Yiming Liu[a], Jingbo Wang[a], Bongyeon Jung[a], Unnati Rao[a], Erfan Sedighi[b], Eric M.V. Hoek[a,c], Nils Tilton[d], Tzahi Y. Cath[e], Craig S. Turchi[f], Michael B. Heeley[g], Y. Sungtaek Ju[b], David Jassby[a*]

[a] University of California Los Angeles (UCLA), Department of Civil & Environmental Engineering, California NanoSystems Institute and Institute of the Environment & Sustainability, Los Angeles, CA, USA
[b] UCLA, Department of Mechanical and Aerospace Engineering, Los Angeles, CA, USA
[c] Energy Science & Distributed Resources Division, Lawrence Berkeley National Laboratory, Berkeley, CA, USA
[d] Colorado School of Mines, Department of Mechanical Engineering, Golden, CO, USA
[e] Colorado School of Mines, Department of Civil and Environmental Engineering, Golden, CO, USA
[f] Buildings & Thermal Science Center, National Renewable Energy Laboratory, Golden, CO, USA
[g] Colorado School of Mines, Department of Economics and Business, Golden, CO, USA

Prepared for

Water Research

November 19, 2021

*Corresponding author [tel: (310) 825-1346; email: jassby@ucla.edu]

Abstract

Membrane distillation (MD) is an emerging thermal desalination technology capable of desalting waters of any salinity. During typical MD processes, the saline feedwater is heated and acts as the thermal energy carrier; however, temperature polarization leads to low distillate fluxes, low single-pass water recovery and poor thermal efficiency. An alternative approach is to integrate an extra thermal energy carrier as part of the membrane and/or module assembly, which can channel externally provided heat directly to the membrane-feedwater interface and/or along the feed channel length. This direct-heat delivery has been demonstrated to increase single-pass water recovery and enhance the overall thermal efficiency. We developed a bench-scale direct-heated vacuum MD (DHVMD) process to desalinate oil and gas "produced water" with an initial total suspended solids of 115,500 ppm at ambient temperatures. We evaluated both water flux and specific energy consumption (SEC) as a function of water recovery. The system achieved an average flux >6 kg m^{-2} hr^{-1}, a SEC as low as 2,530 kJ kg^{-1}, and a maximum water recovery of 68%. The major species of mineral scales (i.e., NaCl, $CaSO_4$, and $SrSO_4$) that limited the water recovery were modeled in terms of thermodynamics and identified by scanning electron microscopy and energy-dispersive X-ray spectroscopy. In addition, we further developed and employed a physics-based process model to estimate temperature, salinity, water transport and energy flows for full-scale vacuum MD and DHVMD modules. Model results show that direct-heat input rate of 3,600 W can increase single-pass water recovery by 48.3% while lowering the thermal SEC by 16.4%. Finally, possible designs for a full-scale DHVMD plant to achieve high water recovery and high gained output ratio values were shown.

Keywords: membrane distillation; hyper-saline water; brine; produced water; mineral scale; process modeling

1. Introduction

Management of hyper-saline waste brines (e.g., total suspended solids (TDS) concentration >70 g L^{-1}) is critical in the oil and gas (O&G) industry and many other industries (Pramanik et al., 2017; Shaffer et al., 2013). To reduce disposal costs (Pramanik et al., 2017) and environmental impacts (Tasker et al., 2018), O&G produced water typically requires treatment using a wide range of technologies to remove oil and grease, suspended solids, and soluble hydrocarbons before reducing salinity (Fakhru'l-Razi et al., 2009; Hoek et al., 2021; Robbins et al., 2020). When brine concentration or minimum liquid discharge (MLD) is a goal, thermal desalination technologies must be used to concentrate the brine up to 250 g L^{-1} TDS (Li et al., 2015). The concentrated brine can be further treated using a thermal salt crystallizer if zero liquid discharge (ZLD) is desired (Chen et al., 2014; Kim et al., 2018; Kim et al., 2017; Tun et al., 2005; Wang et al., 2020).

Membrane distillation is a thermally driven evaporation/desalination process through porous hydrophobic membranes. One advantage of membrane distillation (MD) is that water flux and energy demand are relatively insensitive to TDS concentration, whereas for pressure-driven desalination processes like reverse osmosis (RO), the water flux, salt rejection, and energy demand are directly impacted by TDS concentration. Furthermore, RO is limited to desalination of saline water up to 80 g L^{-1} TDS, whereas MD is capable of treating hyper-saline brines up to the point of saturation (Deshmukh et al., 2018). Another advantage of MD is the high surface area-to-volume ratio of a membrane module, which can lower capital costs compared to conventional thermal desalination processes, particularly for small applications of less than 500 m^3 day^{-1} (<100 gal min^{-1}) (Deshmukh et al., 2018).

In conventional MD, the feed is preheated before entering the membrane module to provide the driving force for vapor transport, which is a partial pressure difference between the feed side and the distillate side of the membrane. During operation, the water vapor leaving the feed, at the feed-membrane interface, contains the latent heat of evaporation that crosses with the vapor into the distillate side of the membrane, which results in a lower temperature at the feedwater-membrane interface, a phenomenon called temperature polarization. The presence of temperature polarization decreases the driving force for evaporation across the membrane by lowering the temperature and therefore partial vapor pressure of the feed stream. Heat is also lost through conduction across the membranes and across the boundaries of the membrane element and other components of the system. Therefore, a thermodynamic limit to water recovery (<10%) in a single-pass MD process is expected for standard operating conditions (Bartholomew et al., 2020; Gilron et al., 2007; Lin et al., 2014).

Delivering heat directly to the feed channel and/or the membrane surface could minimize temperature polarization in a directly heated vacuum MD (DHVMD) system, and thereby increase single-pass water recovery and lower specific energy consumption (SEC). Previous studies have shown that MD systems that incorporate membrane surface heating (e.g., through resistive heating, induction heating, or photothermal heating) can be used for high salinity water desalination (Anvari et al., 2019; Dongare et al., 2017; Dudchenko et al., 2017; Huang et al., 2021; Li et al., 2019). In addition, thermal energy can also be delivered to the bulk feed and the feedwater-membrane interface through conductive transfer of externally supplied heat via thermally conducting materials (e.g., metal plates and meshes) incorporated into the membrane module. In a recent study (Wang et al., 2021), a vacuum MD (VMD) process with direct-heat input rate was evaluated in 2-hour long tests using hypersaline feed water containing 100 g L^{-1}

NaCl under varying operating conditions. The process resulted in water flux as high as 9 kg m^{-2} hr^{-1} and high thermal efficiency, especially with surface heating only.

In this study, we evaluate the performance of DHVMD applied to desalination of a hyper-saline produced water for which the water recovery was limited by mineral scale formation. We identify the principal mineral scale forming species via thermodynamic modeling, scanning electron microscopy (SEM) and energy-dispersive X-ray spectroscopy (EDS). We also report the SEC as a function of water recovery in the lab-scale DHVMD module. In addition, we perform full-scale simulations to compare the performance of a standard VMD and DHVMD modules in desalting a hyper-saline brine. Through the model, we explore the impacts of direct-heating on temperature and concentration polarization, water flux, heat flux, water recovery, and thermal SEC. Finally, we show possible designs for a full-scale DHVMD plant to achieve high water recovery and high gained output ratio (GOR) values.

2. **Materials and Methods**

2.1. MD membrane and thermally conducting materials

The membranes used for DHVMD are hydrophobic polypropylene (PP) membranes (3M, Charlotte, NC) with an average thickness of 100 μm, an average pore size of 0.2 μm, and a porosity of 70%. We consider two types of thermally conductive layers. The first is a thin aluminum sheet (shim) placed on the feed channel wall opposite the membrane, as shown in Fig. 1c. The second is an aluminum mesh that is in direct contact with the membrane in the distillate channel (McMaster-Carr, Los Angeles, CA), also as sketched in Fig. 1c. The aluminum shim had a thickness of 250 μm, and the aluminum mesh had a mesh size of 120×120 (109 μm opening

size), a thickness of 203 μm, and a 27% open area. The membrane coupon, aluminum shim piece, and aluminum mesh piece were cut from flat sheets obtained from the manufacturers and used directly without further modification.

2.2. Feed characterization and preparation

The experiments used high salinity produced water as feed. The water was effluent from a membrane bioreactor (MBR) used to treat the water, with the raw feed to the MBR collected from O&G extraction wells in the Permian Basin. The main water quality characteristics of the produced water are listed in Table S1. Inorganic species with the highest concentration were found to be Na^+ and Cl^-, which were at least 10 times higher than any other inorganic constituents. In addition to inorganic constituents, the produced water had low levels of dissolved organic carbon (DOC), because the majority of organics contaminates were removed during the MBR process.

Based on the water quality information, we used the OLI stream analyzer (OLI systems Inc., Cedar Knolls, NJ) to quantify the thermodynamic tendency of salt precipitation using the unitless saturation index. The saturation index of inorganic species $C_x A_y$ was calculated using Eq. 1:

$$SI = \frac{(a_C)^x (a_A)^y}{K_{sp}(C_x A_y)} \quad (0)$$

where a_c is the activity of cation C, a_A is the activity of anion A, and $K_{sp}(C_x A_y)$ is the solubility product of $C_X A_y$. The indices for cation activity and anion activity follow the stoichiometry of the inorganic salt. When SI exceeds 1, the solution is supersaturated with respect to the particular mineral, and precipitation will take place spontaneously. The OLI simulations were performed using estimates for the salinity and temperature at the membrane surface. The membrane surface

156 salinity and temperature were approximated using the concentration polarization factor (CP) and
157 the temperature polarization factor (TP) predicted by the full-scale process model (see details in
158 Section 2.6). The thermodynamics modeling provides an estimate of salt precipitation tendency
159 at the membrane interface.

160 The produced water used for the experiments was either used directly or pre-concentrated by
161 50% using a rotary vacuum evaporator (Thermo Fisher Scientific, Waltham, MA); no noticeable
162 crystallization of inorganic salts was observed during pre-concentration. In terms of the
163 evaporator's operating conditions, the water bath temperature was set to 55 °C, the vacuum was
164 provided by a whole-house vacuum system located in the UCLA engineering building
165 (approximately 0.8 bar absolute pressure), and the rotational speed was set to 180 rpm.

166

167 ***2.3. DHVMD experiments***

168 Fig. 1a shows a flow diagram of the batch DHVMD system used to desalinate the produced
169 water. Flux measurements were performed by measuring changes in the mass of the feed tank
170 holding the produced water (Ohaus, Model Number PX2202, Parsippany, NJ). Feed mass
171 measurements were performed every 5 second. The feed was circulated through the membrane
172 module using a peristaltic pump (Cole Parmer, Vernon Hills, IL) or a gear pump (Greylor, Cape
173 Coral, FL), both of which have speed/flow control. A cartridge filter with a 1 μm pore size
174 (Hydronix, Chino Hills, CA) in the recirculation line after the outlet of the membrane module,
175 was used in the experiments where the pre-concentrated produced water was further treated. This
176 filter was used to capture any precipitates formed from homogeneous nucleation in the feed tank
177 (Zhang et al., 2015). Temperature sensors (Vktech, Shenzhen, China) were placed in the inlet
178 and outlet of the flow cell to monitor the feed temperature in real time. The temperature sensors

were controlled via an Arduino microcontroller. The flow cell was constructed of polyether ether ketone (PEEK), a polymer known for its ability to withstand high temperatures. The length, width, and height of the flow channel were 4 cm, 10 cm, and 4 mm (or 3 mm), respectively. During cross-flow operation, room-temperature feed was pumped into the membrane module and evaporation took place at the feedwater-membrane interface. A vacuum pump (JB Industries, Model Number DV-85N, Aurora, IL) was used to induce vacuum on the distillate side to drive water vapor transport across the membrane. The vacuum was set at 0.01 bar absolute pressure, as measured by an external vacuum pressure gauge (McMaster-Carr, Los Angeles, CA). The vapor produced by the cell and passed to a condenser (Chemglass Life Sciences, Vineland, NJ) in which the coolant (50 wt.% ethylene glycol at 0 °C) was recirculated using a refrigerated bath circulator (Thermo Fisher Scientific, Waltham, MA). The distillate was then collected in a flask.

The coupling of the thermal energy supply to the shim and mesh is illustrated in Fig. 1b. A cartridge heater with an internal temperature sensor (McMaster-Carr, Los Angeles, CA) provided the thermal energy. The heating temperature was regulated by a thermostat (Inkbird, Shenzhen, China). In this setup, the mesh and shim funnel the externally provided heat to the membrane/water interface (mesh) or into the feed channel itself (shim). Type K thermocouples (AWG 24, Minnesota Measurement Instruments LLC, Minnesota, MN) were mounted to the surfaces of the mesh and the shim by Kapton tape (McMaster-Carr, Los Angeles, CA) to measure the temperature at different points on the shim and the mesh, as previously detailed in Wang *et al.* (Wang et al., 2021). Detailed arrangement of feed streams, membrane materials and module, and both heat and water flows inside the module is presented in Fig. 1c.

Rate of Heat flow to the membrane surface or feed channel delivered through the thermally conducting layers, $\dot{Q}_{heat}$ (W), was estimated by (Wang et al., 2021)

$$\dot{Q}_{heat} = -k_{eff} A \frac{\Delta T}{\Delta x} \quad (0)$$

where k_{eff} (W m^{-1} K^{-1}) is the thermal conductivity of the thermally conducting layer, A (m^2) is the cross-sectional area of the thermally conducting layer, and ΔT (K) and Δx (m) are the temperature difference and the distance between two specified points on the thermally conducting layer along the direction of heat transfer, respectively.

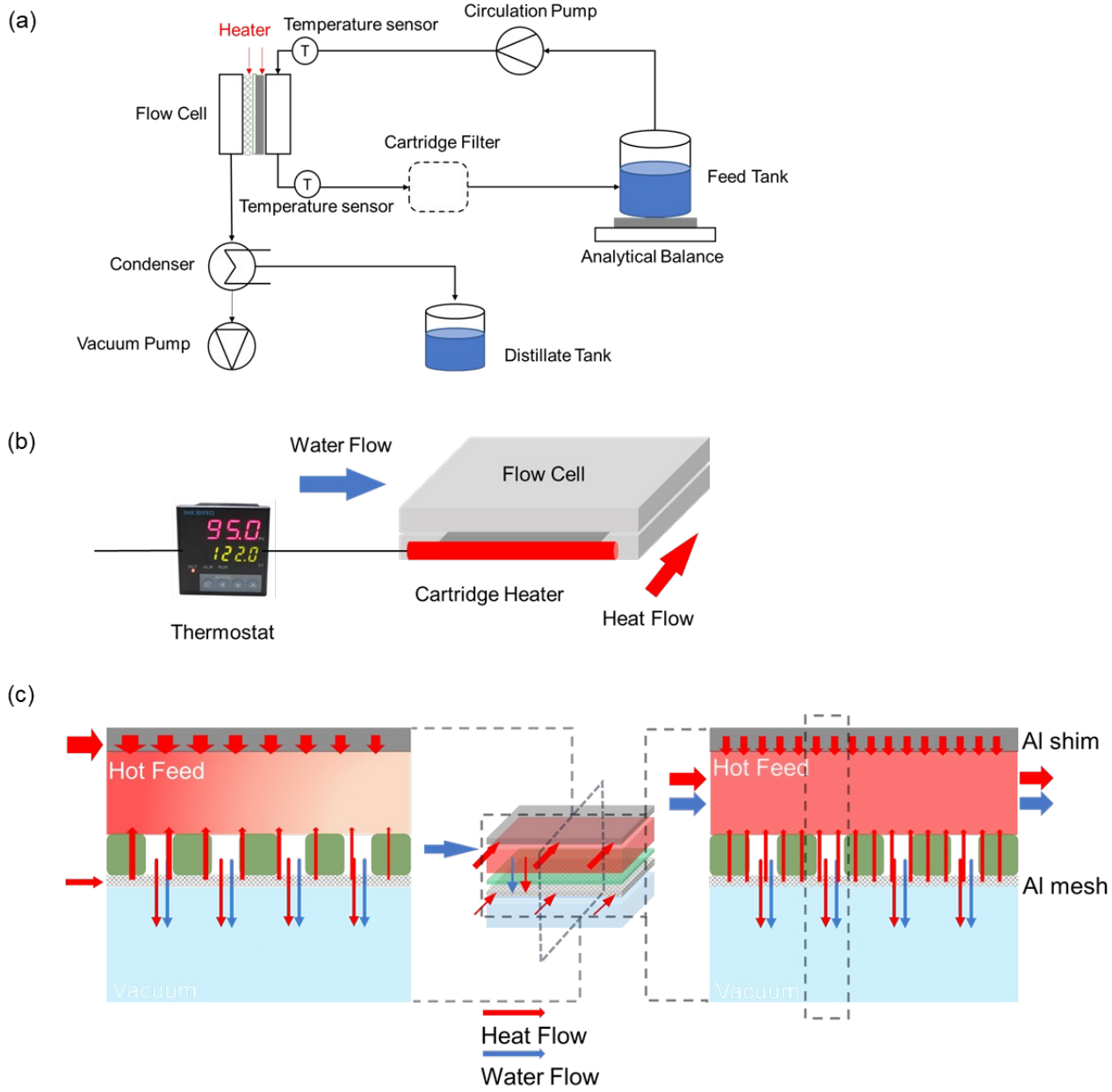

Fig. 1. (a) Flow schematic of the bench-scale DHVMD system. The PEEK membrane flow cell houses a flat sheet membrane, and thermal conductors that are coupled with heater. (b) Schematic of the coupling between thermal conductors in the flow cell and heat source. In specific, flat-sheet thermal carriers (both mesh and shim) were wrapped around a cartridge heater. Red arrows denote heat flows and blue arrows denote water flows. (c) Schematic of heat and mass transfer in two-dimensional cross sections of a three-dimensional membrane module. The left cross section is parallel to the *x*-*z* plane and the right cross section is parallel to the *y*-*z* plane. Along the membrane, the heat is fed from one side through the shim and the mesh. The shim conducts the heat to the feed at the bottom of the feed channel, and the mesh conducts the heat to the feedwater-membrane interface. Across the membrane, the water evaporation at the feedwater-membrane interface creates water and heat flows from the feed side to the distillate side.

To explore the impact of water recovery on performance, the system was operated in a recirculating mode that constantly recirculated feed through the module, while the distillate was not returned to the feed tank, which allowed the concentrations of rejected constituents to increase over time. Water recovery in MD is typically defined as the percentage of the feed that becomes distillate. In this lab-scale MD system, the water recovery (Y) was defined from

$$Y = \frac{\Delta m}{m} \tag{0}$$

where Δm (g) is the cumulative water production represented by the reduction in feed mass between 0 and certain recovery, and m (g) is the initial feed mass. Each of the experiments was terminated at the target value of Y, and then the process performance metrics such as distillate flux and salt rejection were computed. The distillate flux, J (kg m^{-2} hr^{-1}), was calculated as

$$J = \frac{\dot{m}}{A_m} \tag{0}$$

where $\dot{m}$ (kg hr^{-1}) is the decreasing rate of feed mass and A_m (m^2) is the effective membrane area. For each set of experiments, the distillate flux was calculated using the slope of the linear regression of the feed mass change over time, divided by the effective membrane area, at different recoveries. Each data point of feed mass used for flux calculation was an average of all the measurements in 10 minutes. The electrical conductivities of the feed and the distillate were

235 determined using a conductivity meter and conductivity cell (Thermo Fisher Scientific, Waltham,
236 MA), which can measure the electrical conductivity (as high as 200 mS m^{-1}) in high salinity
237 environments. The measured electrical conductivities are used to calculate the salt rejection (R)
238 as

$$R = 1 - \frac{c_d}{c_f} \quad (0)$$

239 where c_d and c_f are the electrical conductivities of the distillate and feed, respectively.

240 Experiments were conducted in triplicate to evaluate the system behavior in terms of flux as a
241 function of water recovery under the following range of operating conditions (Table 1). Each
242 feed mass value was selected to provide the minimized duration based on experimental
243 conditions. Among all the conditions, the feed mass variable had limited impact on the
244 performance regardless of scaling.

245
246 **Table 1**. Experimental conditions for all the sets of experiments

# of Experimental Condition	Recovery	Feed Mass (g)	Heat Source Temperature (°C)	Feed Crossflow Velocity ($cm \cdot s^{-1}$)	Addition of Cartridge Filter
1	0-50%	500	140	16	No
2	0-50%	300	180	16	No
3	0-68%	300	180	22	No
4	50%-66%	1200	180	22	Yes

247

248 ***2.4. Membrane characterization***

249 The membranes were examined to characterize the layers of mineral scale that developed on
250 their surface using SEM (Zeiss Supra 40 VP, Carl Zeiss Microscopy LLC, NY). Quantitative
251 analysis and surface elemental mapping were also carried out using EDS to determine the type

and species of mineral scale. Before imaging, samples were secured on SEM stubs using double-sided carbon tape, and sputter coated with platinum.

2.5. DHVMD system energy performance

The energy requirements in a typical VMD system consist of three components (Mericq et al., 2011): thermal energy for feed evaporation, the electrical energy for vacuum generation, and the electrical energy for feed recirculation. For the calculation of the thermal energy demands, we assume that our experimental system operated with no environmental losses, considering the flow cell is made up of heat insulating material. The energy efficiency of an MD system was evaluated using SEC as a metric based on the quantities of total energy consumed and the quantity of water being treated.

SEC (kJ kg^{-1}) was defined as the amount of total energy supplied (thermal energy and electrical energy in this case) to produce a cumulative mass of pure water, which can be calculated using (Miladi et al., 2019):

$$SEC = STEC + SEEC \tag{0}$$

where STEC (kJ kg^{-1}) is the specific thermal energy consumption, which can be calculated as (Soomro and Kim, 2018)

$$STEC = \frac{\dot{Q}_{heat} \times 10^{-3}}{\frac{\Delta m}{\Delta t}} \tag{0}$$

where Δt (s) is the corresponding time interval between 0 and a certain recovery. SEEC (kJ kg^{-1}) is the specific electrical energy consumption defined as the electrical energy consumed ($\dot{E}$, kJ s^{-1}) to produce a unit mass of pure water:

$$SEEC = \frac{\dot{E}}{\frac{\Delta m}{\Delta t}} \tag{0}$$

The electrical energy consumption is composed of the energy needed to create vacuum on the distillate side and to circulate the feed. The method used to calculate the electrical energy input $\dot{E}$ (kJ s^{-1}) is detailed in Wang *et al.* (Wang et al., 2021).

2.6. Module-scale DHVMD model

Numerical simulation of an MD process at a module scale provides important insights into the spatial distributions of temperature, salinity, and water and energy flows along the membrane (Deshmukh and Elimelech, 2017; Gustafson et al., 2016; Lin et al., 2014; Ma et al., 2018). In the DHVMD model used here, the governing equations of momentum transport, mass transport, and heat transport and the property relations were coupled to generate a prediction of the conditions along the membrane surface. The governing equations, computational approach, and validation against experimental results are detailed in the Supplementary Information (SI) (Section S2). A major difference between traditional VMD models and the model used here is the addition of heat to the non-membrane side of the feed channel and/or the feedwater-membrane interface using the energy carriers (e.g., metal plates for conductive heating or electrically conducting layer for electric heating). To approximate the actual conditions, we discretize the membrane module in the longitudinal direction to create 10,000 differential segments (a single discretized section is represented by the dashed line box in the right cross section in Fig. 1c). The first-order Euler method (a type of finite difference method) was used to translate this system of non-linear differential equations to a system of linear equations that can be calculated based on the inputs of influent feed conditions, operational parameters, channel dimensions, and membrane properties (see Section S2 for details).

3. Results and Discussion

3.1. Heat delivery and distribution

The initial feed temperature in all experiments was room temperature, which was 24±0.5 °C. Under all the experimental conditions, the feed temperature rapidly increased during the initial recoveries, reaching the steady-state temperature at 31.5 °C (see Section S3). Heat in the DHVMD system was provided entirely by thermal conduction through the aluminum mesh and/or shim. Based on Eq. 5, the total heat input rate from both the shim and mesh was determined to be 16.3±1.8 W and 21.7±2.6 W, when the heat source temperatures were set to 140 °C and 180 °C, respectively (Table 2). The heat input rate from the shim was more than 10 times higher than that from mesh, given the similar temperature gradient, due to the shim's greater thermal conductance, which was a result of the materials' larger cross-sectional area.

Table 2. Heat delivery by aluminum shim and aluminum mesh to the membrane module based on the temperature data measured using thermocouples taped on shim and mesh.

Heat Source Temperature (°C)	Temperature Change on Shim (K m^{-1})	Heat Input Rate from Shim (W)	Temperature Change on Mesh (K m^{-1})	Heat Input Rate from Mesh (W)	Total Rate of Heat Input Rate (W)
140	19.7 ± 2.3	15.2 ± 1.8	16.9 ± 0.5	1.0 ± 0.03	16.3 ± 1.8
180	26.1 ± 3.2	20.2 ± 2.5	25.5 ± 5.1	1.5 ± 0.38	21.7 ± 2.6

When the DHVMD reached steady state, most heat delivered to the membrane module was used for evaporation and/or to heat up the bulk feed, as the heat lost to the environment was minimized by supplying and consuming heat *in situ*, evidenced by the high thermal efficiency of DHVMD in Wang *et al.* (Wang et al., 2021). As thermal energy carriers, the shim and the mesh functioned differently in terms of driving the DHVMD process, as they were placed at different locations inside the membrane module. The shim is positioned on the feed channel wall opposite

315 the membrane and provided heat to the flowing feed stream in a manner similar to the feed
316 preheating in conventional MD systems. In contrast, the mesh was placed under the membrane
317 (distillate side and in direct contact with the membrane), and provided heat directly to the
318 membrane/feed interface. In this configuration, the porous mesh allows water vapor to pass
319 through the membrane and into the distillate channel. Because the thermal conductivity of the
320 water vapor is an order of magnitude smaller than that of the liquid water, heat generated from
321 the mesh is delivered primarily across the membrane to convert liquid water to vapor.
322
323 ***3.2. Water flux vs. recovery***
324 A set of experiments that concentrated the produced water using different operating
325 conditions (conditions 1 and 2 in Table 1) was performed to achieve 50% water recovery, and
326 vapor flux was measured as a function of water recovery (Fig. 2a). Over the course of the
327 experiments (from 0 to 50% recovery) the flux increased up to 10% recovery and then fluctuated
328 between 4.7±1.6 kg m^{-2} hr^{-1} and 6.3±0.2 kg m^{-2} hr^{-1} when T_H = 140 °C. The flux exhibited the
329 similar initial increase and then fluctuated between 5.0±0.4 kg m^{-2} hr^{-1} and 7.4±0.6 kg m^{-2} hr^{-1}
330 when T_H = 180 °C (Fig. 2a). These results showed that 50% recovery could be achieved with
331 stable flux and little scaling. Higher heat source temperature resulted in greater heat input rate
332 (Table 2), so the system exhibited higher flux. To explore system performance at higher feed
333 salinity, we evaluated higher distillate recovery and terminated the experiments when the flux
334 dropped below 1 kg m^{-2} hr^{-1}. This occurred at approximately 66% to 68% recovery (Fig. 2b,
335 condition 3 in Table 1 with T_H at 180 °C). Overall, the flux firstly increased (from 4.4±1.2 kg m^{-2}
336 h^{-1} to 7.8±1.5 kg m^{-2} h^{-1}) up to 10% recovery, then gradually declined (from 7.8±1.5 kg m^{-2} h^{-1} to
337 6.9±0.4 kg m^{-2} h^{-1}) up to about 50% recovery, and after 50% recovery flux declined dramatically

(from 6.9±0.4 kg m^{-2} h^{-1} to 2.3±2.0 kg m^{-2} h^{-1}). The relatively unstable flux measurements above 50% recovery were likely due to the onset of mineral scaling via heterogeneous crystal nucleation and growth on the membrane combined with homogeneous precipitate deposition and sloughing along the surface. A cartridge filter was used to further investigate flux behavior beyond 50% recovery (condition 4 in Table 1). The flux became far more stable (Fig. 2b, red data points), which suggested that some homogeneous crystallization indeed occurred. However, we still observed a rapid flux decline as the system approached 60% recovery, with the flux dropping from 4.8±0.3 kg m^{-2} hr^{-1} at 60% recovery to 0.1±0.1 kg m^{-2} hr^{-1} at about 66% recovery. At a recovery greater than 60%, the feed had a salinity about 3 times higher than its original concentration, which was close to the solubility limit of NaCl in the bulk and even higher near the membrane surface due to CP even with a higher temperature at the feedwater-membrane interface. The rapid formation of minerals at these high recoveries can block the pores through the membrane and prevent water vapor from passing into the distillate channel.

We modeled the DHVMD process using the experimental parameters as inputs and found the average TP and CP (defined in Eqs. S25 and S32) to be 0.988 and 1.32, respectively. Those factors were used to compute the membrane surface temperature and salinity based on the bulk feed temperature (Section 3.1) and salinity (Table S1). We then determined that NaCl exceeded its saturation indices at 60% recovery (Fig. 2c), which corresponded to the rapid onset of flux decline. In addition, $SrSO_4$, $CaSO_4$, and $CaSO_4 \cdot 2H_2O$ were already saturated below 50% recovery, but because the concentrations of Sr and Ca were relatively low, the formation of these crystals did not have a dramatic impact on system performance, but perhaps played a role in the gradual flux decline from 10% to 50% recovery. Previous literature suggests rapid crystal growth by supersaturated NaCl and slower growth for $CaSO_4$ and $SrSO_4$ (Kiefer et al., 2019).

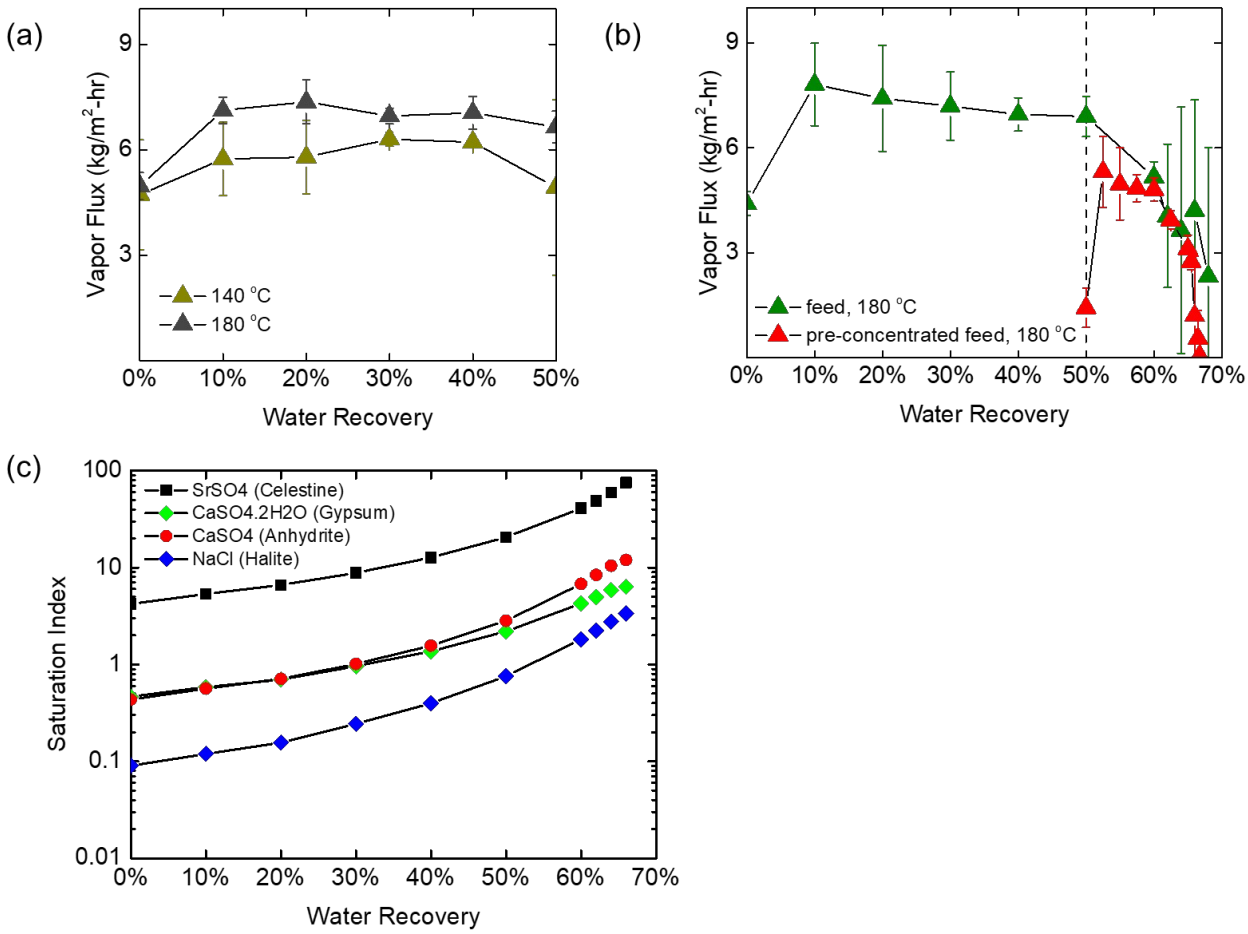

Fig. 2. Water flux versus recovery (a) from 0 to 50% with different feed heat source temperature (T_H = 140 °C, dark gray data points; T_H = 180 °C, dark yellow data points), and (b) from 0 to 68% (olive data points) and 50% to 66% (red data points). (c) Saturation indices of different scale-forming species (celestine, black data points; gypsum, green data points; anhydrite, red data points; halite, blue data points) at the feedwater-membrane interface versus water recovery from 0 to 66%. All the tests performed have a salt rejection above 99.9%.

SEM micrographs and EDS analysis of pristine MD membranes and those used in experiments are shown in Fig. 3. Both SEM micrographs and EDS data showed that there was limited inorganic fouling when water recovery was below 50% (Figs. 3a and 3b). The lack of crystals on the membrane surface when recovery reached 50% was in line with the stable flux observed when recovery was below this level (Figs. 2 and 3). In addition, $SrSO_4$ crystals were not observed despite the fact that the saturation indices of both salts suggested that precipitation

should take place. However, at 68% recovery, the membrane was covered by a large number of crystals of varying morphology, including needle-like (likely $CaSO_4$ and $SrSO_4$) and cubic crystals (likely NaCl) (Figs. 3c and 3d). EDS analysis of these images revealed the presence of Na, Cl, Sr, Ca, S, and O confirming the formation of NaCl, $SrSO_4$, $CaSO_4$ species. A detailed EDS mapping analysis of the membrane surface can be found in the SI (Fig. S3). Overall, the characterization results from both the SEM and EDS, together with the OLI simulations, suggested that the precipitation of NaCl predominantly caused the flux decline at recovery above 50%.

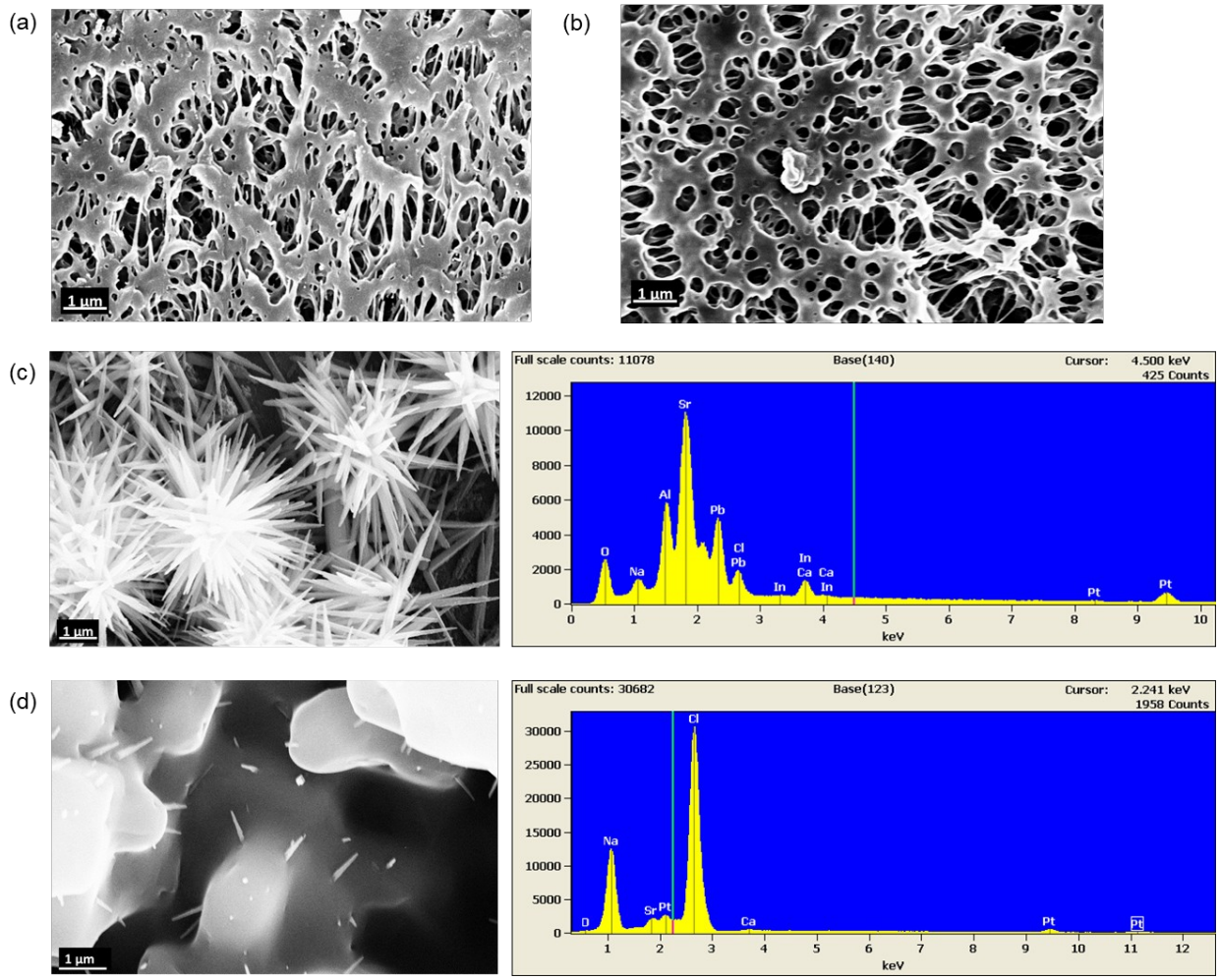

Fig. 3. (a) SEM image of a pristine PP membrane surface; (b) SEM image of used PP membrane from the experiment at 50% water recovery; (c) and (d) SEM image and the corresponding EDS

spectrum of two different spots of the used PP membrane from the experiment with 68% water recovery. In the EDS spectrum, the x-axis is energy (keV), and the y-axis is counts for element.

3.3. Specific energy consumption vs recovery

The SEC, STEC, and SEEC as a function of the % recovery were calculated to quantify the system energy performance. In the lab-scale system without any heat recovery, the SECs of desalination were consistent with previously reported energy consumption values (Wang et al., 2021), which demonstrated that the DHVMD system had a lower SEC than other MD techonologies. Overall, the STEC is the larger component of the SEC, while the SEEC makes up only a small part of the SEC, with the STEC being markedly higher than the SEEC by 2-3 orders of magnititude (Fig. 4). Therefore, the SEC analysis is focused primarily on the STEC. Under all conditions tested, the STEC decreased and eventually reached a steady state as the recovery increased; thus we focused our discussion on these steady state conditions.

Figs. 4a and 4b present the SEC (STEC + SEEC) as a function of water recovery from 0 to 50% with different heat source temperatures (conditions 1 and 2 in Table 1). Under these conditions, scaling was limited, the flux was relatively stable (Fig. 2a), and the STEC was steady when recovery ranged between 10% and 50% (Figs. 4a and 4b). When T_H = 140 °C, and water recovery increased from 10% to 50%, the STEC decreased from 2,720±158 kJ kg^{-1} to 2,530±81 kJ kg^{-1}. When T_H increased to 180 °C, the system had a higher STEC, with the STEC between 10% and 50% recovery ranging between 3,068±140 kJ kg^{-1} and 2,897±123 kJ kg^{-1} (Fig. 4b). The increase in STEC was because the increased culmulative water production rate (which increased with increasing heat input rate) was smaller than the increased heat input rate at the higher temperature (i.e., the heating was less efficient) (Eq. 7).

To investigate the impact of scaling on system energy peformance, Figs. 4c and 4d plot the SEC (STEC + SEEC) as a function of water recovery above 50%, where membrane scaling was observed and the membrane experienced rapid flux decline (conditions 3 and 4 in Table 1). Beyond 50% recovery, the STEC values remained stable until 60% recovery was reached. However, at 60% recovery the STEC began increasing due to a dramatic flux decline (Figs. 4c and 4d). The flux decline decreased the culumulative water production, and thus increased STEC. Because the system has a high stable flux for a relatively long time before flux decline, the STEC did not have a marked increase, as shown in Figs. 4c and 4d.

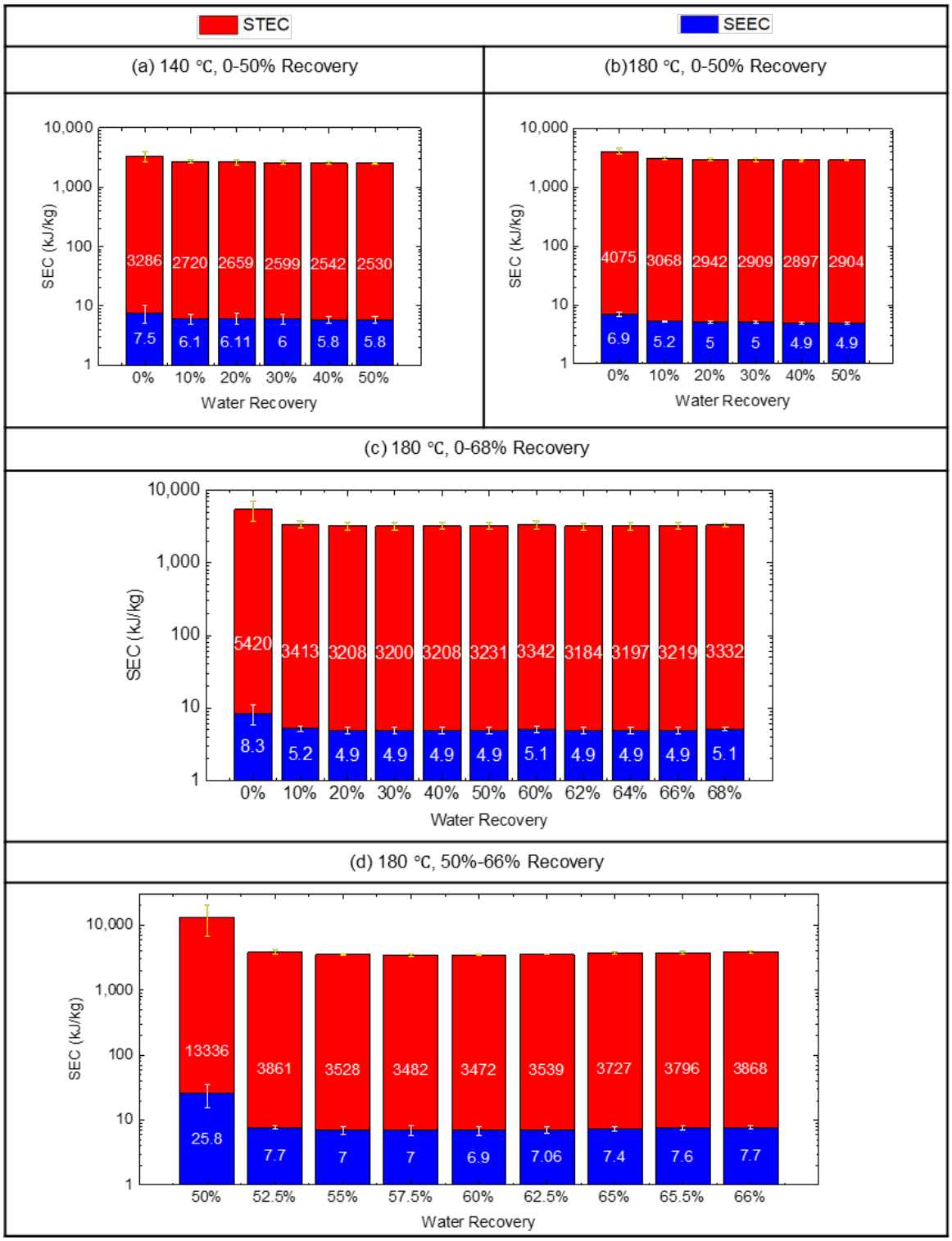

Fig. 4. SEC, STEC, and SEEC as a function of recovery from 0 to 50% (a) when T_H = 140 °C, (b) when T_H = 180 °C, (c) from 0 to 68% when T_H = 180 °C, and (d) from 50% to 66% when T_H = 180 °C. The red bars represent the STEC and the blue bars represent the SEEC, and the sum of STEC and SEEC is equal to SEC.

The STEC is negatively impacted by scaling, as shown in Fig. 4. The formation of mineral scale blocked the vapor flow through the membrane, resulting in lower cumulative water production rate and higher STEC values. With scale formation that prevents feed from evaporating, the supplied heat was primarily used to heat up the bulk feedwater in the feed channel based on the heat distribution shown in Section 3.1. The increased feed temperature could decrease the solubility of mineral species such as $CaSO_4$ and $SrSO_4$, which further affect the SEC performance. Therefore, to achieve good STEC performance, it is necessary to target maximum water recovery while preventing scale formation.

3.4. DHVMD process modeling

Our experimental results demonstrated the feasibility of a lab-scale DHVMD process for concentrating real O&G produced water. To explore potential performance of a full-scale DHVMD process, we simulated a full-scale module. The simulation captures temperature, salinity, water transport, and energy flows during the steady-state operation of a single-pass DHVMD system. Operating conditions, module dimensions, feed solution properties, and membrane properties used in the simulation are described in the SI (Table S2). We used the model to compare the performance of a standard VMD process (no heat addition) to the DHVMD process (with the addition rate of 3,600 W of heat to the membrane surface, 3,600 W of heat to the feed channel, or 1,800 W of heat to the membrane surface and 1,800 W heat the feed channel).

Membrane surface temperature and bulk feed temperature profiles for the module are calculated for both the VMD and DHVMD systems (Fig. 5a). Membrane surface heating increases the membrane surface temperature the most, followed by hybrid heating (heating both

membrane surface and feed channel) and feed channel heating, with the same amount of total heat input rate (3,600 W). Not surprisingly, feed channel heating is most effective at increasing the bulk feed temperature given the same heat input rate, followed by hybrid heating and membrane surface heating. The average TP for the entire module is plotted in Fig. 5b as the ratio of membrane surface and bulk feedwater temperature (Eq. S25). Throughout the entire module, membrane surface heating increased the TP while feed channel heating reduced the TP. Hybrid heating resulted in a net increase in the TP, which shows that membrane surface heating impacts temperature polarization more than feed channel heating does.

The longitudinal profiles of bulk feed salinity and the salinity of the feed along the membrane surface are shown in Fig. 5c. The salinity at the feedwater-membrane interface is most significantly increased by membrane surface heating, followed by hybrid heating and feed channel heating. In contrast, the bulk feed salinity only slightly increases along the module. Fig. 5d presents the longitudinal CP profile for the module, defined as the salinity at the feedwater-membrane interface salinity divided by the bulk feed salinity (Eq. S32). Given the same heat input rate, membrane surface heating increased the concentration polarization to a greater extent, followed by hybrid heating and feed channel heating.

The longitudinal water flux (calculated by Eq. S35) and heat flux (calculated by Eq. S18) from the bulk feed along the length of the module under different heating conditions are shown in Fig. 5e. Membrane surface heating has the highest impact on water flux (increasing it) for a given heat input rate. The vapor flux has the highest increase caused by surface heating, followed by hybrid heating and feed channel heating. In addition to vapor flux, we also evaluate the heat flux. Heat flux characterizes the heat losses of the feed, which is the sum of membrane surface heat input rate and convective heat transfer rate (of vapor). Membrane surface heating

reduces heat losses, feed channel heating increases heat losses, and hybrid heating has a net effect of reducing heat losses for the module.

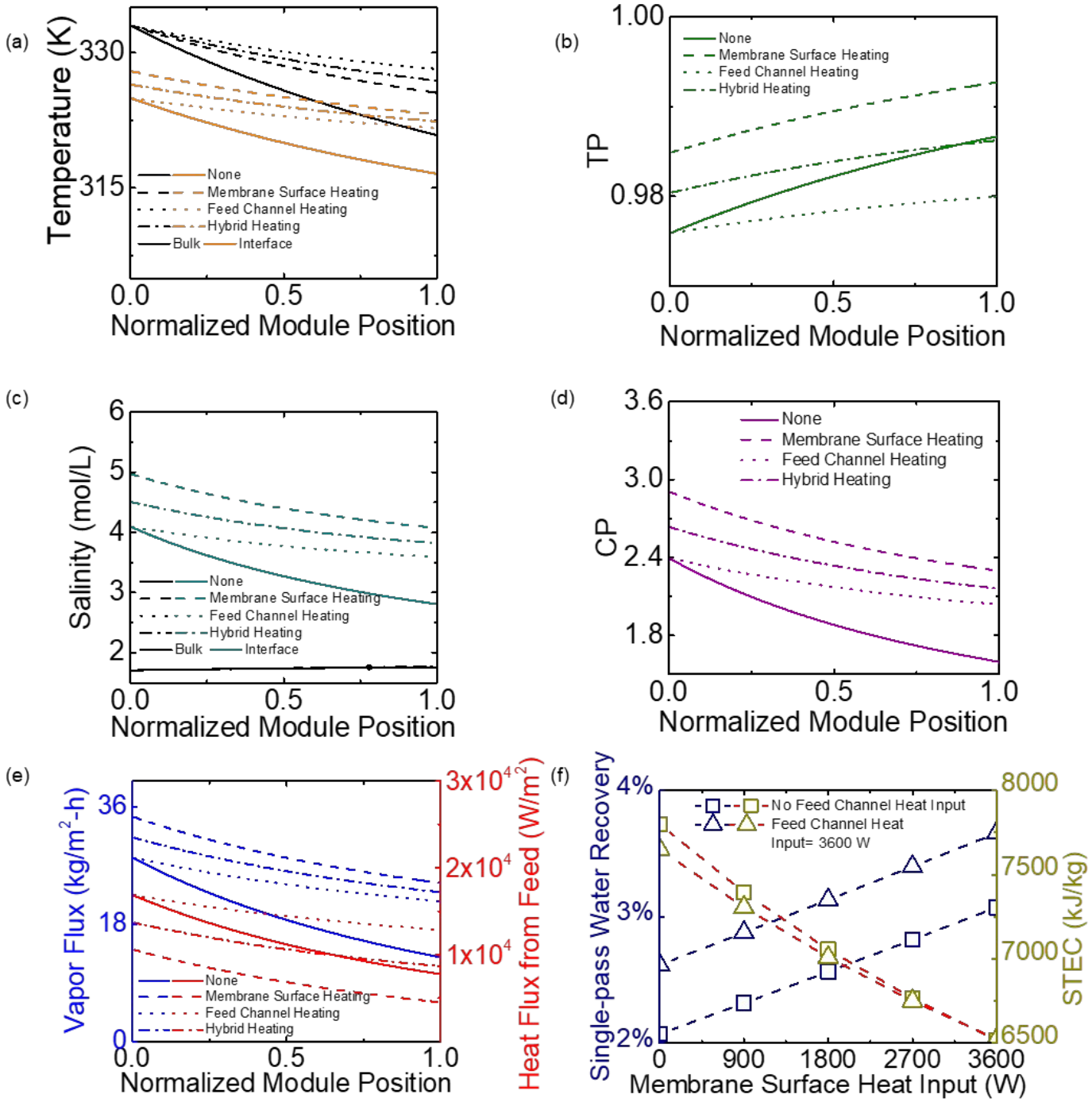

Fig. 5. (a) Membrane surface temperature (orange lines) and bulk feed temperature (black lines), (b) temperature polarization factors (TP, olive lines), (c) membrane surface salinity (dark cyan

lines) and bulk feed salinity (black lines), (d) concentration polarization factors (CP, purple lines), (e) transmembrane water flux (blue lines) and heat flux from bulk feed (red lines) as a function of normalized DHVMD module position with different direct-heating conditions, membrane surface heating (adding 3600 W heat to membrane surface), feed channel heating (adding 3600 W heat to feed channel), and hybrid heating (adding 1800W heat to membrane surface and 1800 W heat to feed channel). The solid lines represent the condition without any heat input while the dashed, dotted, and dashed-and-dotted lines represent membrane surface heating, feed channel heating, and hybrid heating, respectively. (f) Single-pass water recovery (navy blue) and the STEC (dark yellow) of a single-pass DHVMD as a function of heat input rate to membrane surface under different feed channel heating conditions, including no heat input (squares) and heat input rate of 1800 W to feed channel (triangles).

Based on the vapor and heat flux data, we calculate the single-pass water recovery and STEC at a system level for different heat input rates to the membrane surface (from 0 to 3,600 W with an interval of 900 W) and to the feed channel (Fig. 5f). In the STEC calculation of the process model (Eq. S37), heat input rates include the direct-heat input rate as well as the heat input rate required to heat the bulk feed to 60 °C before entering the membrane module. With a heat input rate of 3,600 W to the membrane surface, the single-pass water recovery increases by about 48.3%. The STEC has a 16.4% decrease due to the increased water recovery and reduced heat loss. In comparison, the equivalent heat input rate (3,600 W) to the feed channel increases the single pass water recovery by 26.3%, which is less than the impact of surface heating (48.3%), and yielded nearly no reduction (an 1.9% decrease) in the STEC due to the heat loss divided by water recovery staying the same.

Water recovery can also be further increased under more optimized conditions for heat and mass transfer, such as longer channel length, lower channel depth, higher feed temperature, stronger vacuum, and higher membrane permeability. However, in a single pass MD, it is hard to achieve a water recovery needed for brine concentration, as shown in the previous reports (Lin et al., 2014). Therefore, the DHVMD system requires a single stage batch or semi-batch configuration (our experimental system), or a multi-staged single pass configuration

(Bartholomew et al., 2020; Dudchenko et al., 2021; Mulder, 2012) to achieve a high total water recovery (and concentrate the feed up to 310 g L^{-1} TDS).

To maximize energy efficiency and achieve high GOR values, heat recycling is critical in all thermal desalination systems. DHVMD will be no exception. The minimum work of separation in thermal desalination is the latent heat of vaporization of water, which is 2260 kJ kg^{-1} (Deshmukh et al., 2018). This is far higher than the energy needed for pressure-driven desalination processes (e.g., seawater RO is about 8 to 12 kJ kg^{-1}). Thermal desalination technologies, including MD, consequently use heat exchangers to recover the latent heat of condensation, and lower their overall energy consumption (Bartholomew et al., 2020; Chung et al., 2016; Dudchenko et al., 2021). Large scale thermal desalination processes have GOR values between 10 and 20, with actual STECs as low as 8.3 kJ kg^{-1} (Al-Karaghouli and Kazmerski, 2013; Ihm et al., 2016). It should be noted that even if a GOR of 20 is assumed, at 2260 kJ kg^{-1} the practically achievable minimum work of separation for a thermal process is 113 kJ kg^{-1}, which is an order of magnitude higher than a seawater RO unit including irreversible losses. Hence, thermal desalination makes sense in two scenarios: (1) when oil and gas are extraordinarily cheap and the steam generated by a steam-electric cogeneration power plant can be used to drive the desalination process (as in the Middle East) or (2) when the osmotic pressure of a hypersaline water exceeds the pressure limits of commercially available RO membranes and/or process equipment.

4. **Conclusion**

We developed a bench-scale, batch DHVMD system to desalinate a real O&G produced water with an initial TDS concentration of 115,500 mg L^{-1} TDS. We achieved a maximum of 66% water recovery at an average water flux >6 kg m^{-2} hr^{-1}, an overall salt rejection >99.9%, and a single stage SEC as low as 2530 kJ kg^{-1} (703 kWh m^{-3}). The concentrated brine had a TDS concentration high enough to achieve NaCl saturation, which is often a target in brine concentration processes, with the goal of "minimum liquid discharge". In addition to experimental efforts, we modeled temperature, salinity, water transport, and energy flows in a medium-scale DHVMD module. The results suggest that an addition rate of 3,600 W of thermal energy to the feedwater-membrane interface increases water recovery by 47.6% and decreases the STEC by 16.4% in a single pass. We further discussed possible designs of a large scale DHVMD for brine concentration that use batch/multistage configuration and incorporate heat recovery systems, to achieve high water recovery and high gained output ratio. The DHVMD process demonstrated herein shows promise for eventual scale-up in the desalination of high-salinity O&G produced water and other hyper-saline waters.

Declaration of Competing Interest

The authors declare that they have no known competing financial interests or personal relationships that could have appeared to influence the work reported in this paper.

Acknowledgements

The SEM and EDS analyses were conducted at the California NanoSystems Institute, Los Angeles, California, 90095, USA. This work is supported by the Department of Energy (DOE) (Award No. DE-EE0008391) and the Sustainable LA Grand Challenge (EMVH). The authors thanks Mr. Brett Van Houghton for pre-treating the produced water for this study.

References

Al-Karaghouli, A. and Kazmerski, L.L. 2013. Energy consumption and water production cost of conventional and renewable-energy-powered desalination processes. Renewable and Sustainable Energy Reviews 24, 343-356.

Anvari, A., Kekre, K.M., Yancheshme, A.A., Yao, Y. and Ronen, A. 2019. Membrane distillation of high salinity water by induction heated thermally conducting membranes. Journal of Membrane Science 589, 117253.

Bartholomew, T.V., Dudchenko, A.V., Siefert, N.S. and Mauter, M.S. 2020. Cost optimization of high recovery single stage gap membrane distillation. Journal of Membrane Science 611, 118370.

Chen, G., Lu, Y., Krantz, W.B., Wang, R. and Fane, A.G. 2014. Optimization of operating conditions for a continuous membrane distillation crystallization process with zero salty water discharge. Journal of membrane science 450, 1-11.

Chung, H.W., Swaminathan, J., Warsinger, D.M. and Lienhard, J.H. 2016. Multistage vacuum membrane distillation (MSVMD) systems for high salinity applications. Journal of Membrane Science 497, 128-141.

Deshmukh, A., Boo, C., Karanikola, V., Lin, S.H., Straub, A.P., Tong, T.Z., Warsinger, D.M. and Elimelech, M. 2018. Membrane distillation at the water-energy nexus: limits, opportunities, and challenges. Energy & Environmental Science 11(5), 1177-1196.

Deshmukh, A. and Elimelech, M. 2017. Understanding the impact of membrane properties and transport phenomena on the energetic performance of membrane distillation desalination. Journal of Membrane Science 539, 458-474.

Dongare, P.D., Alabastri, A., Pedersen, S., Zodrow, K.R., Hogan, N.J., Neumann, O., Wu, J., Wang, T., Deshmukh, A. and Elimelech, M. 2017. Nanophotonics-enabled solar membrane distillation for off-grid water purification. Proceedings of the National Academy of Sciences 114(27), 6936-6941.

Dudchenko, A.V., Bartholomew, T.V. and Mauter, M.S. 2021. Cost optimization of multi-stage gap membrane distillation. Journal of Membrane Science 627, 119228.

Dudchenko, A.V., Chen, C., Cardenas, A., Rolf, J. and Jassby, D. 2017. Frequency-dependent stability of CNT Joule heaters in ionizable media and desalination processes. Nat Nanotechnol 12(6), 557-563.

Fakhru'l-Razi, A., Pendashteh, A., Abdullah, L.C., Biak, D.R.A., Madaeni, S.S. and Abidin, Z.Z. 2009. Review of technologies for oil and gas produced water treatment. Journal of hazardous materials 170(2-3), 530-551.

Gilron, J., Song, L. and Sirkar, K.K. 2007. Design for cascade of crossflow direct contact membrane distillation. Industrial & engineering chemistry research 46(8), 2324-2334.

Gustafson, R.D., Murphy, J.R. and Achilli, A. 2016. A stepwise model of direct contact membrane distillation for application to large-scale systems: Experimental results and model predictions. Desalination 378, 14-27.

Hoek, E.M., Wang, J., Hancock, T.D., Edalat, A., Bhattacharjee, S. and Jassby, D. 2021. Oil & Gas Produced Water Management. Synthesis Lectures on Sustainable Development 2(1), 1-91.

595 Huang, J., He, Y. and Shen, Z. 2021. Joule heating membrane distillation enhancement with
596 multi-level thermal concentration and heat recovery. Energy Conversion and
597 Management 238, 114111.
598 Ihm, S., Al-Najdi, O.Y., Hamed, O.A., Jun, G. and Chung, H. 2016. Energy cost comparison
599 between MSF, MED and SWRO: Case studies for dual purpose plants. Desalination 397,
600 116-125.
601 Kiefer, F., Präbst, A. and Sattelmayer, T. 2019. Membrane scaling in Vacuum Membrane
602 Distillation-Part 2: Crystallization kinetics and process performance. Journal of
603 Membrane Science 590, 117293.
604 Kim, J., Kim, J. and Hong, S. 2018. Recovery of water and minerals from shale gas produced
605 water by membrane distillation crystallization. Water research 129, 447-459.
606 Kim, J., Kwon, H., Lee, S., Lee, S. and Hong, S. 2017. Membrane distillation (MD) integrated
607 with crystallization (MDC) for shale gas produced water (SGPW) treatment. Desalination
608 403, 172-178.
609 Li, J., Guan, Y., Cheng, F. and Liu, Y. 2015. Treatment of high salinity brines by direct contact
610 membrane distillation: Effect of membrane characteristics and salinity. Chemosphere
611 140, 143-149.
612 Li, K., Zhang, Y., Wang, Z., Liu, L., Liu, H. and Wang, J. 2019. Electrothermally Driven
613 Membrane Distillation for Low-Energy Consumption and Wetting Mitigation. Environ
614 Sci Technol 53(22), 13506-13513.
615 Lin, S., Yip, N.Y. and Elimelech, M. 2014. Direct contact membrane distillation with heat
616 recovery: Thermodynamic insights from module scale modeling. Journal of membrane
617 science 453, 498-515.
618 Ma, Q., Ahmadi, A. and Cabassud, C. 2018. Direct integration of a vacuum membrane
619 distillation module within a solar collector for small-scale units adapted to seawater
620 desalination in remote places: Design, modeling & evaluation of a flat-plate equipment.
621 Journal of Membrane Science 564, 617-633.
622 Mericq, J.-P., Laborie, S. and Cabassud, C. 2011. Evaluation of systems coupling vacuum
623 membrane distillation and solar energy for seawater desalination. Chemical Engineering
624 Journal 166(2), 596-606.
625 Miladi, R., Frikha, N., Kheiri, A. and Gabsi, S. 2019. Energetic performance analysis of
626 seawater desalination with a solar membrane distillation. Energy Conversion and
627 Management 185, 143-154.
628 Mulder, J. (2012) Basic principles of membrane technology, Springer Science & Business
629 Media.
630 Pramanik, B.K., Shu, L. and Jegatheesan, V. 2017. A review of the management and treatment
631 of brine solutions. Environmental Science: Water Research & Technology 3(4), 625-658.
632 Robbins, C.A., Grauberger, B.M., Garland, S.D., Carlson, K.H., Lin, S., Bandhauer, T.M. and
633 Tong, T. 2020. On-site treatment capacity of membrane distillation powered by waste
634 heat or natural gas for unconventional oil and gas wastewater in the Denver-Julesburg
635 Basin. Environment International 145, 106142.
636 Shaffer, D.L., Arias Chavez, L.H., Ben-Sasson, M., Romero-Vargas Castrillón, S., Yip, N.Y. and
637 Elimelech, M. 2013. Desalination and reuse of high-salinity shale gas produced water:
638 drivers, technologies, and future directions. Environmental science & technology 47(17),
639 9569-9583.

Soomro, M.I. and Kim, W.-S. 2018. Performance and economic investigations of solar power tower plant integrated with direct contact membrane distillation system. Energy conversion and management 174, 626-638.

Tasker, T., Burgos, W., Piotrowski, P., Castillo-Meza, L., Blewett, T., Ganow, K., Stallworth, A., Delompré, P., Goss, G. and Fowler, L. 2018. Environmental and human health impacts of spreading oil and gas wastewater on roads. Environmental science & technology 52(12), 7081-7091.

Tun, C.M., Fane, A.G., Matheickal, J.T. and Sheikholeslami, R. 2005. Membrane distillation crystallization of concentrated salts—flux and crystal formation. Journal of Membrane Science 257(1-2), 144-155.

Wang, J., Liu, Y., Rao, U., Dudley, M., Ebrahimi, N.D., Lou, J., Han, F., Hoek, E.M., Tilton, N. and Cath, T.Y. 2021. Conducting thermal energy to the membrane/water interface for the enhanced desalination of hypersaline brines using membrane distillation. Journal of Membrane Science 626, 119188.

Wang, Z., Deshmukh, A., Du, Y. and Elimelech, M. 2020. Minimal and zero liquid discharge with reverse osmosis using low-salt-rejection membranes. Water research 170, 115317.

Zhang, P., Knötig, P., Gray, S. and Duke, M. 2015. Scale reduction and cleaning techniques during direct contact membrane distillation of seawater reverse osmosis brine. Desalination 374, 20-30.